Design and Validation of a Partial-Assist Knee Orthosis with Compact, Backdrivable Actuation

Hanqi Zhu[1,2], Christopher Nesler[2], Nikhil Divekar[2], M. Taha Ahmad[1,2], and Robert D. Gregg[2,3]

***Abstract*— This paper presents the mechatronic design and initial validation of a partial-assist knee orthosis for individuals with musculoskeletal disorders, e.g., knee osteoarthritis and lower back pain. This orthosis utilizes a quasi-direct drive actuator with a low-ratio transmission (7:1) to greatly reduce the reflected inertia for high backdrivability. To provide meaningful assistance, a custom Brushless DC (BLDC) motor is designed with encapsulated windings to improve the motor's thermal environment and thus its continuous torque output. The 2.69 kg orthosis is constructed from all custom-made components with a high package factor for lighter weight and a more compact size. The combination of compactness, backdrivability, and torque output enables the orthosis to provide partial assistance without obstructing the natural movement of the user. Several benchtop tests verify the actuator's capabilities, and a human subject experiment demonstrates reduced quadriceps muscle activation when assisted during a repetitive lifting and lowering task.**

I. INTRODUCTION

Traditionally, exoskeletons (i.e., powered orthoses) aid paraplegic individuals with little to no remnant voluntary movement, e.g., following a severe stroke or spinal cord injury [1], [2]. As a result, many exoskeleton designs have focused on achieving high torque output to fully support the lower extremities. However, larger populations of individuals with musculoskeletal disorders would benefit from partial assistance of their musculature rather than full assistance. This includes 27 million individuals with osteoarthritis [3] and 66 million individuals with lower back pain [4] in the USA alone. Weak quadriceps musculature is a significant contributing factor to the persistence and progression of both conditions, a limitation that can potentially be resolved by assistive knee torques. In the case of knee osteoarthritis, this assistance would in turn reduce high forces at the patellofemoral and tibiofemoral joints, ultimately reducing pain [5], [6]. Likewise, lower back pain that results from repetitive lifting and lowering (L&L) tasks could potentially benefit from partial assistance, as fatigued quadriceps contribute to poor posture in these tasks [7]. To achieve partial assistance, several design goals must be balanced: 1) facilitation of non-hindered voluntary movement of the user (high backdrivability), 2) a non-cumbersome design (light weight, compact), and 3) capacity to provide meaningful torque assistance to the user.

[1]Department of Electrical and Computer Engineering, [2]Department of Bioengineering, [3]Department of Mechanical Engineering. University of Texas at Dallas, Richardson, TX 75080, USA. rgregg@ieee.org

This work was supported by the National Institute of Child Health & Human Development of the NIH under Award Number DP2HD080349 and the National Science Foundation under Award Number 1652514. The content is solely the responsibility of the authors and does not necessarily represent the official views of the NIH or the NSF. This work was also supported by a gift from The Philip R. Jonsson Foundation. R. D. Gregg holds a Career Award at the Scientific Interface from the Burroughs Wellcome Fund. The work of Hanqi Zhu was supported by the Eugene McDermott Graduate Fellowship.

Backdrivability is defined as the ratio between the actuator's output torque and its backdrive torque [8]. There are several methods to achieve high backdrivability, e.g., closed-loop force control of a series elastic actuator (SEA) [9]–[12]. However, SEAs tend to have limitations such as low output torque [9], complex system architecture [13], [14], large size/weight [15], and/or limited force/torque control bandwidth [16]. The powered knee orthosis in [8] uses a hydraulic actuator to achieve high backdrivability without sacrificing output torque, but electric motors tend to be much more efficient than hydraulic actuators. In recent years, legged robots have used torque-dense electric motors with low transmission ratios (i.e., quasi-direct drive actuators) to achieve highly dynamic motions, compliance to impacts, regenerative braking, and accurate torque control [17]–[19]. Backdrivability is maximized by minimizing the reflected inertia of the actuator, which can be improved by increasing the torque output of the electrical motor and reducing the transmission ratio [17]. However, electric motors need high currents to generate sufficient torque output, producing tremendous heat. A forced liquid cooling system can be used to reduce the motor winding temperature, which dramatically increases the motor's torque output capability [20]. However, the liquid cooling system, including its pump, adds significant mass and bulk, making this approach less desirable for exoskeletons used in the home or community.

Our previous work [21] implemented a torque-dense electric motor with a low (24:1) transmission ratio in a backdrivable knee-ankle exoskeleton intended for stroke rehabilitation, which has high torque requirements. This actuator had a static backdrive torque of 1.5 Nm and a peak dynamic backdrive torque of 8 Nm during walking [22]. However, the previously discussed thermal condition was the main factor limiting the rated peak (60 Nm) and continuous (30 Nm) output torques of the actuator. This exoskeleton was also too bulky and heavy (4.88 kg), and possibly overdesigned, for everyday use by individuals with musculoskeletal disorders. By further reducing the gear ratio to 8.55:1 (and sacrificing output torque), Su et al. [23] recently implemented a highly backdrivable, partial-assist knee orthosis using a torque-dense electric motor. However, the continuous torque of 6 Nm may be insufficient for more demanding activities (e.g., stair climbing, or repetitive L&L, see Section II). The distributed actuator design may also make this orthosis too heavy (3.2 kg) and bulky for everyday use.

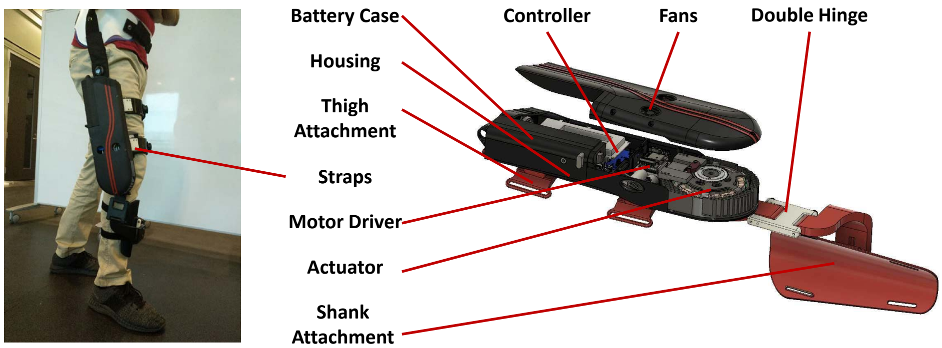

Fig. 1. Photo and CAD model of the powered knee orthosis. The shank attachment, which incorporates a double hinge as well as other linear and angular adjustments, allows for a wide range of leg curvatures to experience a comfortable fit. The CAD model is built and rendered using Fusion 360.

Weight and size are important design constraints for a partial-assist knee orthosis. Most exoskeletons use off-the-shelf motors and gearboxes, which lead to low package factors [24]. The package factor is defined as the ratio between the mass of the functional components (e.g., gears, rotor) and the support components (e.g., bearings, frame). For example, the Robodrive motor in the prosthetic leg [25] is 1.3 kg but its core components (stator, rotor) are only 0.37 kg, resulting in a low package factor. To the our knowledge, actuator package factor has not been directly considered in the exoskeleton literature. A higher package factor was achieved in a small legged robot by designing a 6:1 planetary gearbox into the inner diameter of a torque-dense T motor [26]. This lightweight, compact design achieved a peak torque of 17 Nm and a continuous torque of 5 Nm, but the latter may be insufficient for human assistance.

In this paper we demonstrate the implementation of two design innovations to improve the backdrivability, weight, and size of a powered knee orthosis (Fig. 1). First, we applied encapsulation technology to reduce the motor's winding temperature and thus facilitate higher output torques. Encapsulation is a new packaging method for the motor's stator that provides highly efficient heat transfer from the motor windings to the heat sink [27]. The higher torque density of this motor allows the use of a smaller transmission ratio (7:1), which greatly increases backdrivability. Second, we custom-manufactured all core components of the actuator, designing the planetary gears inside the stator. By sharing the same supporting components, we increased the package factor to 1.5 with a total actuator mass of 1.5 kg. Benchtop experiments verify that the custom actuator has approximately 20 Nm peak torque, 10.62 Nm continuous torque, less than 0.5 Nm static backdrive torque, and less than 1.2 Nm RMS backdrive torque during walking conditions. A preliminary human subject experiment demonstrates a reduction in quadriceps muscle activation while assisted by the knee orthosis during a repetitive L&L task.

II. Actuator Design and Analysis

A. Actuator System Design

A prior study [28] observed reduced knee moments during walking after severe osteoarthritis (OA) when compared to the asymptomatic pool. Peak knee extension and flexion moments were reduced by 15 Nm and 25.6 Nm, respectively. Based on the knee moment waveforms in [28, Fig. 1], we calculated the mean reduction in absolute knee moment to be 7.3 Nm for an 80 kg individual with OA. Furthermore, a study of lifting techniques [29] found that the rectus femoris muscle has 16.24% more activity during squatting, which is biomechanically sound, compared to stooping, which is known to cause lower back injuries. Based on maximum voluntary contraction (MVC) reference data from [30], this translates to a 27.9 Nm increase in knee torque on average. In order to design an orthosis that can both compensate for osteoarthritic deficits and facilitate sound L&L technique, we set the actuator design goals at 10 Nm continuous torque and 20 Nm peak torque.

The ideal actuator for a partial-assist orthosis should strike a balance between torque output, weight, and reflected inertia [21], [22]. Improving the performance of functional components is difficult, since most of the functional components are limited by current material technologies (e.g., gear's mechanical strength, stator core's magnetic saturation). Reducing the weight of supporting components and increasing the package factor is a more practical way to increase the torque density of the actuator. There are several advantages to having a high package factor design: 1) maximizing space usage with custom-designed core components, 2) minimizing supporting components to reduce weight, and 3) avoiding use of unnecessary connection components (e.g., coupler) between different functional components.

We started our high package factor actuator design with the motor type selection. We chose the outer rotor type Brushless Direct Current (BLDC) motor, which can produce higher torque than an inner rotor type BLDC motor, due to a larger air gap [31]. The functional components of an outer rotor motor are the stator and rotor (Fig. 2). We noticed that the outer rotor BLDC motor has a lot of space inside of the stator, which is not utilized in most traditional actuator designs. Consequently, a single-stage transmission can be designed to fit inside the stator to reduce the thickness and weight of the assembly. A variety of transmission styles are available, including cycloid gears [32], harmonic gears [33], and planetary gears [21]. To minimize reflected inertia and thus maximize backdrivability, we chose a single-stage planetary gearset with a 7:1 transmission ratio.

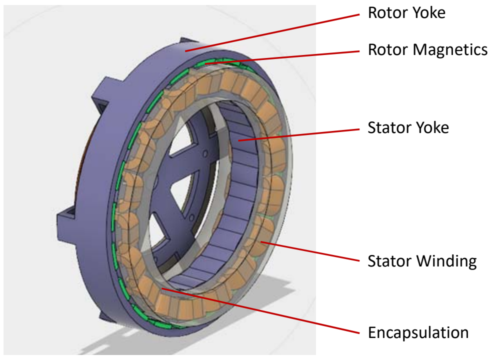

Fig. 2. The presented custom-designed outer rotor BLDC motor. The green parts are the N35 permanent magnets (PMs), the yellow part is the winding, and the transparent part is the encapsulation material. The blue parts are the stator core and the rotor yoke.

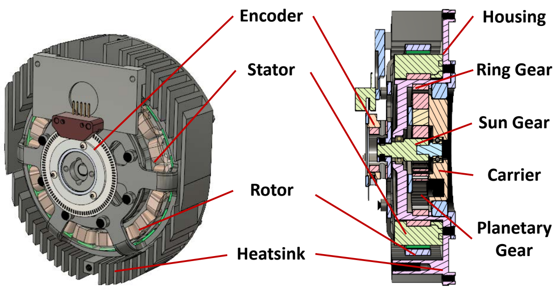

Fig. 3. The presented actuator with a high package factor design. A single-stage planetary transmission is nested inside of the stator. The housing supports both the stator and ring gear. The high package factor design can reduce the total weight and size of the actuator.

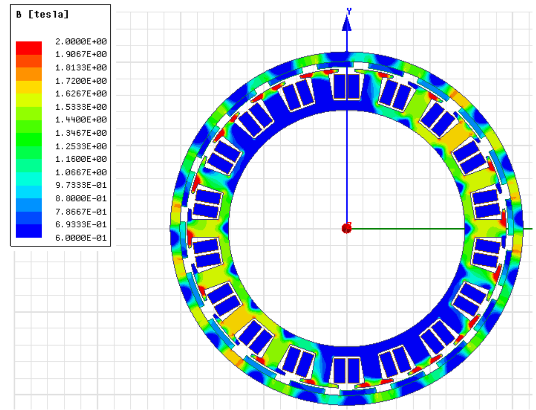

Fig. 4. The rotor magnetic field design. There is no current in the winding for this simulation. By using a high performance magnetic material (Hiperco 50) to build the stator, the magnetic strength of the stator can reach 2.4 T.

TABLE I

PARAMETERS OF DESIGNED OUTER ROTOR MOTOR

Rated power [W]	220.0
Rated speed [RPM]	760.0
No load speed [RPM]	1106.3
Rated torque [Nm]	1.5
Copper loss [W]	44.3
Core loss [W]	2.8
Efficiency [%]	82.3
Phase-phase DC resistance [mOhm]	108.2
Phase-phase inductance (@1kHz) [mH]	0.212
Phase RMS current [A]	17.4
Current density of winding [A/mm^2]	10.5
Rotor inertia [kg-cm^2]	4.1

B. Transmission and Motor Design

The whole gearset is built inside the motor and shares the same housing (Fig. 3). The ring gear is attached to the inner surface of the housing and the sun gear is directly attached to the rotor output shaft. Three planetary gears, engaged with the ring gear and the sun gear, amplify the torque and transfer it to the carrier, which is the output of the actuator. The estimated efficiency of this transmission is 91.9% based on [34]. With the designed transmission ratio of 7:1, the motor needs to produce 1.42 Nm continuous torque to realize the desired continuous actuator torque of 10 Nm. This was achieved by designing a custom BLDC motor with encapsulation technology (Fig. 2).

The torque generated by a BLDC motor is caused by two magnetic fields: the rotor magnetic field (generated by permanent magnets) and the stator magnetic field (generated by current flowing through the winding). The permanent magnets are made of a ferromagnetic material, e.g., silicon steel. This kind of material exhibits a phenomenon called magnetic saturation [35], a state reached when an increase in the applied external magnetic field cannot increase the magnetization of the material further. Consequently, the magnetic flux density of the motor plateaus. The magnetic saturation limits the torque density of BLDC motors and causes highly nonlinear characteristics [36]. To prevent magnetic saturation, we used a special Cobalt alloy (Hiperco 50) to build our BLDC motor [37]. The saturated magnetic flux density of this Hiperco 50 material reaches 2.4 T, which is 33% higher than the saturated flux density of silicon steel (1.8 T). The magnetic flux density of the designed motor is shown in Fig. 4.

The stator magnetic field is produced by the winding current. In this motor, we chose the concentration, fractional-slot type winding (18 slots, 20 poles). The fractional slot design can reduce the cogging torque and decrease the length of the winding, which minimizes copper loss [38]. The current density of our winding design is 10.5 A/mm^2. The motor design can theoretically produce a continuous torque of approximately 1.5 Nm, which will be verified in Section IV. Other motor parameters are given in Table I.

With the custom motor and transmission, the package factor of the presented actuator is 1.5, i.e., 673 g of functional components vs. 447 g of supporting components. Only three bearings are used in this design and the main housing provides support to both the motor and gears. Noting that reflected inertia can be approximated by the rotor inertia times the square of gear ratio [17], the presented actuator has a reflected inertia of 200.9 kg-cm^2. This value is 3.5 times lower than our previous orthosis design with 692.0 kg-cm^2 [21]. Key specifications of the presented actuator are listed in Table II and verified in Section IV.

TABLE II

PARAMETERS OF DESIGNED QUASI-DIRECT DRIVE ACTUATOR

Rated power [W]	198
Rated speed [RPM]	108.57
No load speed [RPM]	158.0
Rated torque [Nm]	9.94
Transmission Ratio	7:1
Reflected Inertia (kg-cm^2)	200.9
Weight (kg)	1.15

C. Thermal System Design

There are two contributions to a motor's heat production: coil heat and core heat. Coil heat is produced from the current passing through the copper wire of the winding. This is also called the Joule loss or the copper loss. The core heat is produced from the stator core due to eddy current, which is generated by a rotational magnetic field. For a quasi-direct drive actuator, the core loss can be ignored due to the relatively low running speed. The majority of the heat in a quasi-direct drive actuator is coil heat.

In our design, the motor produces 44.3 W of copper loss during continuous torque output, which has the potential to burn the windings. The main cause of this damage is the slot insulation, an insulation layer between the winding and the stator. This insulation layer is typically made of a material with poor thermal conductivity, e.g., nylon. As a result, the heat from the winding is very difficult to transfer to the environment, even with a heat sink on the stator case. To solve this problem we applied encapsulation technology to improve the motor's thermal environment [27]. Encapsulation uses a material with high thermal conductivity to fill the air gaps between the core and the winding, which can distribute the heat from the winding to the stator directly. This is an improvement over solely transferring heat through the insulation layer, which has poor thermal conductivity. Our encapsulated stator is shown in Fig. 5 (right). With the help of encapsulation technology, we designed a heat sink around the stator case (Fig. 3) to transfer heat from the stator to the environment through fan openings in the front of the outer nylon case (Fig. 1). Note that the stator/heat sink are separated from the human user by the motor mount, nylon case, and leg attachments, providing multiple layers of insulation to prevent discomfort or harm to the user.

Fig. 5. A comparison between a stator with (right) and without (left) encapsulation technology. Left: a stator without encapsulation, where the white part is the isolation layer made of nylon material. Right: the designed stator with encapsulation, which is the black material.

III. Design of Orthosis System

This section presents the design of a powered knee orthosis with the previously discussed actuator. In this section, the details of the mechanical system, electrical system, and torque control system are introduced. A photo and rendering of the powered knee orthosis are shown in Fig. 1.

A. Mechanical System Design

The designed orthosis connects to the user's knee joint and provides assistive torques that are beneficial during ambulation and other daily activities. A 3D-printed mechanical housing, in conjunction with four straps, is used to secure the orthosis to the user's thigh and lower leg. The produced torque from the actuator transfers through the mechanical housing and the straps to the user.

From the actuator output, the shank attachment contains several adjustable linkage components to provide additional degrees of freedom for optimal adjustment to differences in user anatomy. These linkages terminate in an end effector that fits to the user's leg like an athletic shin guard. A double hinge mechanism was included between the actuator output and the shank attachment, allowing for the position of the end effector to conform more properly to the user's leg while still transferring torque in the sagittal plane. This double hinge design element is also present in the work of Su et al. [23].

B. Electrical System Design

A motor driver (Gold Solo Twitter, Elmo Motion, Inc.) was selected and fixed in the orthosis housing to control the electric motor. Two pancake-shape fans were connected to the top cover of the case to cool the motor driver and actuator. A micro-controller (TMS320F28379D, Texas Instruments, Inc.) was selected to implement a control algorithm and collect real-time feedback data. A 2800 mAh battery (ProLite X, Thunder Power, Inc.) was selected to provide energy for the actuator and the electrical system for 2 hours of continuous operation. A removable nylon case was designed to house the battery.

The motor driver receives the rotor angle from an incremental encoder (E2 Optical, 4096 CPR, US Digital, Inc.) and communicates this data to the controller through Controller Area Network (CAN bus) communication. The controller estimates the joint angle based on the rotor angle and transmission ratio. To implement various torque control methods (e.g., [22], [39]), an Inertial Measurement Unit (3DM-GX4-25, LORD MicroStrain, Inc.) was chosen and installed in the case. Two force sensors (FlexiForce A301, Tekscan, Inc.) were placed inside the shoe to detect stance phase or swing phase during gait. The electrical system is shown in Fig. 6.

C. Low-Level Torque Control

An actuator's torque output T (Nm) is often estimated through the motor's excitation current I (A) according to

$$T(I) = k \cdot I - T_f, \tag{1}$$

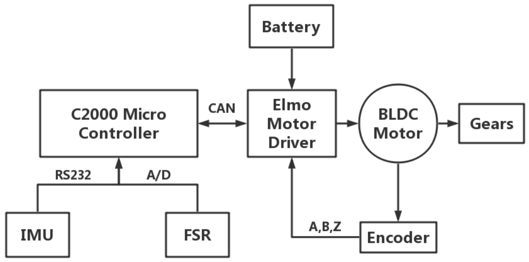

Fig. 6. Schematic of the electrical system for the powered knee orthosis. The C2000 controller receives IMU and force sensitive resistor (FSR) feedback. A quadrature incremental encoder provides position information through signal channels A, B, and Z. By implementing a high level controller, a torque command is sent to the Elmo driver for controlling the motor torque.

where k denotes the actuator's torque constant (Nm/A), and T_f (Nm) accounts for the system's combined losses due to electrical and mechanical inefficiencies. The exoskeleton's high-level controller uses (1) to determine the reference motor current needed to achieve the desired output torque. The high-level controller sends this reference current to the motor driver, which tracks it using a proportional-integral (PI) control loop.

The actuator's torque constant itself depends on the motor's torque constant, the transmission ratio, and the transmission efficiency. In traditional actuators, the transmission efficiency (and thus the torque constant) tends to vary during dynamic motion, causing inaccurate torque estimates from (1). This error is often compensated using torque sensors for closed-loop torque control [21]. Fortunately, quasi-direct drive actuators tend to have a higher, more constant transmission efficiency [17], [22], resulting in better torque estimates from (1). The actuator's torque constant will be identified in Section IV, which will allow the powered orthosis to employ current-based torque control, without the use of a torque sensor.

D. High-Level Control System

To validate the orthosis design, we implemented a *quasi-stiffness* controller for a L&L task. This method provides a virtual spring at the joint based on the slope of a desired torque-angle relationship [40], [41]. Quasi-stiffness directly maps the measured joint angle to the command torque, providing a simple high-level controller for the purpose of validation. We utilized quasi-stiffness control during the stance phase and commanded zero torque during swing phase to allow free motion. The torque control law is given by

$$u = \begin{cases} K\theta & \text{if stance} \\ 0 & \text{if swing} \end{cases}$$

where θ is the measured knee angle with flexion defined in the positive direction. The quasi-stiffness value $K = 0.17$ Nm-deg^{-1} was chosen to deliver 15 Nm assistance torque at 90 deg knee flexion (typical maximum knee angle during a squat lift). Although this controller was designed for a L&L task, future work will implement a task-invariant controller for supporting the various activities of daily life [22].

IV. Experiments and Results

This section presents several experiments to demonstrate the actuator torque output capabilities, thermal properties, backdrivability, and feasibility for human assistance. Benchtop experiments were conducted on an actuator test platform (Fig. 7), which comprised the actuator, a rotational torque sensor (TRS605, FUTEK Advanced Sensor Technology, Inc.), and a magnetic powder brake (351 ELEFLEX, Re Controlli Industriali). The rotational torque sensor measured the actuator's output torque, and the magnetic powder brake fixed the output shaft for applicable tests. An able-bodied human subject experiment demonstrated the potential benefit of the device during a repetitive L&L task. A supplemental video of the experiments is available for download.

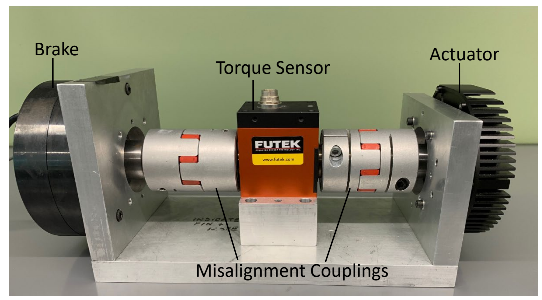

Fig. 7. The actuator test platform includes a magnetic powder brake (left), a FUTEK torque sensor (center), and two misalignment couplings. The actuator (right) is mounted to the testbed frame by its housing, with an output shaft connecting the transmission to the misalignment coupling. The brake is similarly attached on the opposing side of the load cell.

A. Torque Constant Test

We used a series of current step inputs to verify the custom actuator's peak torque, linearity, torque constant, and offset as defined in (1). We fixed the actuator's output shaft, increased the motor's active current from 0 to 35 A in 5 A increments, and recorded the output torques from the torque sensor. Fig. 8 shows that the torque output reached 20.0 Nm with a linear relationship to current (0-35 A). A linear fit estimated the torque constant as 0.59 Nm/A with an offset of -0.21 Nm, which can be used to implement a current-based torque controller in the quasi-direct drive system.

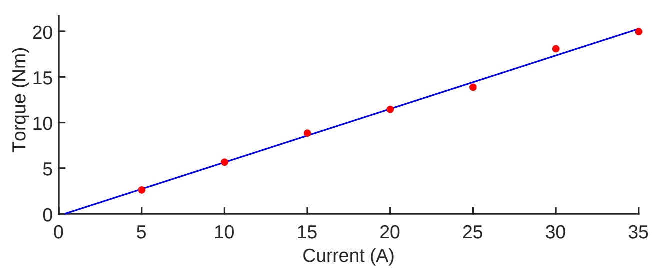

Fig. 8. Output torque measured over a range of current inputs (5-35 A) to identify the actuator torque constant and verify peak torque. Torque constant (0.59 Nm/A) and offset (-0.21 Nm) computed by fitting the data (red) with linear regression (blue).

B. Torque Step Response Test

To verify the actuator's tracking performance using the current-based torque controller, a step response test was conducted. We stepped up the excitation current from 3 A (pre-load) to 30 A and recorded the torque response (Fig. 9). The actuator accurately tracked the reference torque with a steady-state error of approximately 0.08 Nm (measured by the mean difference over the last 0.25 s of Fig. 9). The rise time was found to be 5.2 ms from this test. Assuming second-order actuator dynamics, this rise time implies a natural frequency of 55.1 Hz, which approximates the actuator torque bandwidth within a factor of 2 [42].

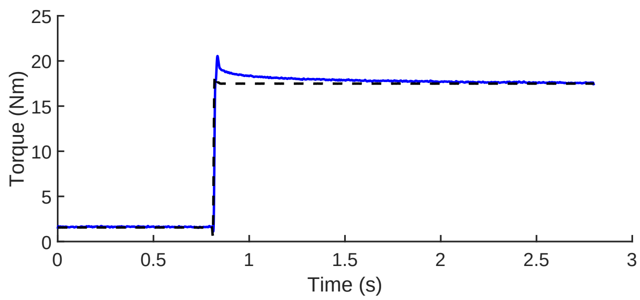

Fig. 9. Results from the continuous torque step response test. Torque values shown are from torque sensor readings (blue), and command current reference (black, dashed). The output torque measured by the FUTEK torque sensor was low-pass filtered (Butterworth, third order, 100 Hz cutoff) for presentation in this figure, but was left unfiltered for the rise time calculation.

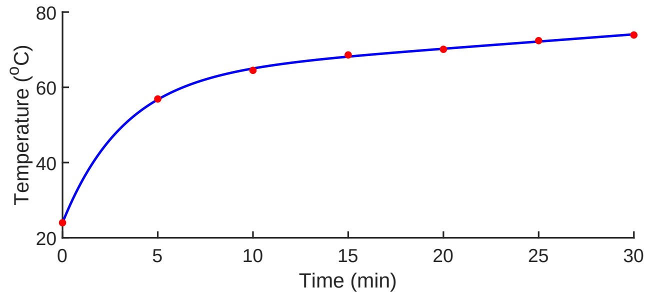

Fig. 10. The temperature curve over 30 minutes of continuous motor operation at 18 A. Maximum stator temperature was recorded at five minute intervals (red), and fit with a two term exponential curve (blue).

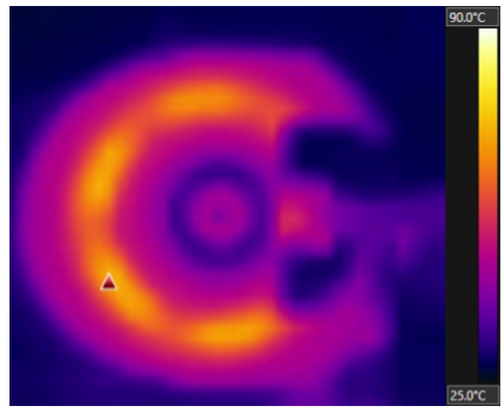

Fig. 11. Thermal image after 30 min of continuous operation. The triangular marker indicates the software-identified point of maximum temperature.

C. Continuous Operating Test

The continuous output torque of an actuator is highly limited by the motor's winding temperature, which motivated our use of encapsulation technology with a heat sink. A continuous operation test was conducted to verify the motor's temperature at the desired continuous output torque (at least 1.5 Nm before the transmission and 10 Nm after it). The actuator was mounted to the test platform with its output shaft fixed by the magnetic brake. We set the operating time to 30 min and kept the actuator continuously running with an excitation of 18 A and used a thermal camera (C2 Compact Thermal Imaging System, FLIR) to measure the stator's surface temperature. After 30 min of operation, the motor's stator surface reached a steady-state temperature of approximately 80 °C (Fig. 10). A thermal camera image at 30 min is shown in Fig. 11. At steady state we can assume the stator surface temperature is equal to the winding temperature. The measured temperature was much lower than the winding burn temperature (150 °C). This experiment demonstrates that the presented actuator can produce a continuous output torque of 10.62 Nm, based on the previously observed torque constant.

D. Backdrivability Tests

The static backdrive torque is defined as the minimum torque required to overcome the static friction of the actuator to initiate motion of its output shaft. A torque was manually applied to the output shaft through a torque wrench (03727A 1/4-inch Drive Beam Style, Neiko) and gradually increased until rotation began. At this point the torque wrench measured less than 0.5 Nm of backdrive torque.

The dynamic backdrive test was designed to characterize backdrivability during simulated walking. In this test we manually rotated the actuator's output shaft between $\pm 30^\circ$ at frequencies of approximately 1 Hz and 2 Hz on the testbed. The backdrive torque measured by the torque sensor was processed using a third-order, low-pass Butterworth filter (10 Hz cutoff) to eliminate sensor noise present at such low torques. The backdrive torque and corresponding angle of the output shaft are shown in Fig. 12. For the 1 Hz portion, the peak backdrive torque was 1.32 Nm, and the RMS backdrive torque was 0.44 Nm. For the 2 Hz portion, the peak and RMS backdrive torques were 2.48 Nm and 1.17 Nm, respectively. We estimate that about 2% of the measured backdrive torque is due to the inertia of the shaft connecting the torque sensor, which would be eliminated in practice.

E. Human Subject Experiment

The human subject experiment was designed to demonstrate the potential benefit of the powered orthosis during a L&L task, i.e., by aiding the quadriceps in the more biomechanically sound squatting technique [29]. We assessed the change in quadriceps muscle activity with orthosis assistance during the L&L task. A single, male human subject (mass: 80 kg, height: 1.78 m) was enrolled for the study which was reviewed and approved by the Institutional Review Board at the University of Texas at Dallas.

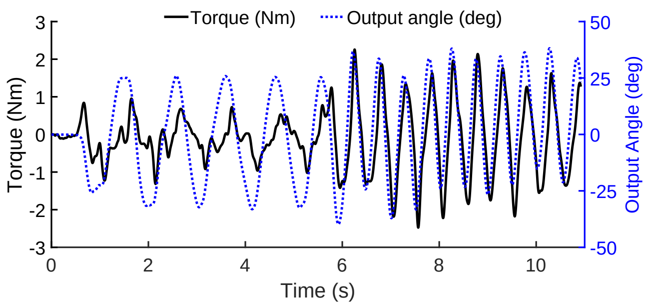

Fig. 12. Dynamic backdrive torque test result. The test platform seen in Fig. 7 was used for this test, in which the left misalignment coupling was manually deflected in a sinusoidal pattern at approximate frequencies of 1 Hz and 2 Hz. The backdrive torque measured by the FUTEK sensor (solid black, left axis) is plotted against the deflection angle measured by the U.S. Digital encoder (dashed blue, right axis).

The L&L task consisted of a repetitive sequence whilst carrying a 20 lb (∼9 kg) mass: 1) standing, 2) lowering, 3) squat hold, and 4) lifting. Each phase lasted 1.5 seconds (cued using a metronome set to 40 BPM). The task was repeated 15 times (3 sets of 5 repetitions) for the three conditions tested: bare (without orthosis), passive (orthosis un-powered) and active (powered orthosis assistance). The passive and active sets were alternated. While the subject was instructed to use a consistent squatting technique, additional controls were set. The positions of the feet were marked and were kept consistent. The subject was instructed to lower the mass until the anterior aspects of both tibias contacted two bars, and the buttocks contacted a horizontal platform (adjusted so femurs were parallel to the floor upon contact). To minimize shifting of weight to any one leg, visual feedback of the vertical ground reaction force of the left leg was provided with the aim of maintaining the force level within a margin marked on-screen.

We used a Delsys system to acquire electromyography (EMG) data from 3 quadriceps muscles: vastus medialis oblique (VMO), rectus femoris (RF), and vastus lateralis (VL) of the right limb, after appropriate skin preparation. An inter-electrode distance of 10 mm was used. MVC data was acquired as the subject maximally contracted his quadriceps against manual resistance. All EMG data was sampled at 2000 Hz and smoothed with a low-pass, zero-lag, second-order Butterworth filter (5 Hz cutoff). L&L trials were normalized with respect to the maximum value in the MVC trial. EMG data corresponding to each repetition was cropped based on the deflection and return to steady state (standing) of the sagittal femur angle (measured using an accelerometer). The cropped trials were then integrated with respect to time to represent muscular effort in Table III. Fig. 13 shows the ensemble average (across repetitions) of time-normalized RF EMG for the three conditions, along with the assistance torque for the active condition. It can be seen that the EMG, and hence muscular effort, was considerably lower for the active orthosis condition compared to both bare and passive orthosis. The difference between passive and bare is negligible in Fig. 13, which can be attributed to the high backdrivability of the actuator. Overall, the

TABLE III

EMG comparisons showing means (± SD) for all conditions

Effort [%MVC.s]	VMO	RF	VL
Bare	90.0 (±10.1)	99.2 (±10.2)	129.7 (±14.2)
Passive	81.4 (±6.2)	102.9 (±12.5)	101.3 (±11.5)
Active	69.5 (±8.4)	70.2 (±7.8)	83.6 (±8.5)

orthosis was able to provide assistive knee torques during the L&L task that in turn reduced the muscular effort of the quadriceps. Further experimentation is needed to determine whether these results translate to users adopting a squatting technique over stooping in the workplace.

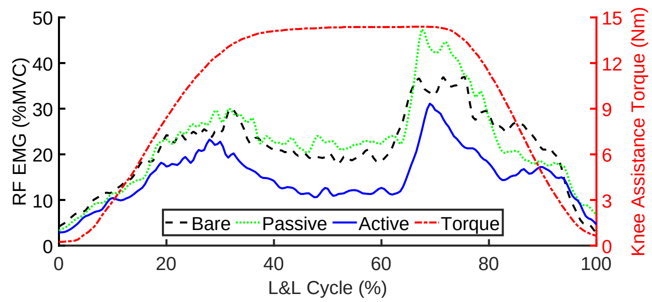

Fig. 13. EMG comparisons between bare, passive, and active modes for RF. The black dashed (bare), green dotted (passive) and blue solid (active) lines represent the time-normalized ensemble averages across the 15 repetitions. The red line represents the time-normalized ensemble average of the commanded torque during active mode.

V. Discussion and Conclusion

This paper presented the design and validation of a partial-assist powered knee orthosis. Compared to our previous research [21], we have improved the thermal environment of the motor through the use of encapsulation technology, allowing for higher torque output. With increased torque output from the motor, we reduced the transmission ratio from 24:1 to 7:1 to decrease the reflected inertia for better backdrivability. The presented orthosis can achieve strong assistance torque (at least 10 Nm continuous torque and 20 Nm peak torque), exhibits low backdrive torque (less than 1.2 Nm RMS), and is lightweight (2.69 kg) with low complexity. Future work will further improve the actuator torque density and ultimately evaluate this partial-assist orthosis in different patient populations to understand its potential clinical benefits.

Competing Interests

Hanqi Zhu is co-founder and shareholder in Enhanced Robotics. These research results may be related to the business interests of Enhanced Robotics. The terms of this arrangement have been reviewed and approved by the University of Texas at Dallas in accordance with its policy on objectivity in research.

Acknowledgments

The authors thank Calvin Stence and Jack Doan for their technical assistance during the early stages of this project and Vamsi Peddinti during the later stages of this project.

REFERENCES

[1] R. J. Farris, H. A. Quintero, and M. Goldfarb, "Preliminary evaluation of a powered lower limb orthosis to aid walking in paraplegic individuals," *IEEE Trans. Neural Systems and Rehabilitation Engineering*, vol. 19, no. 6, pp. 652–659, Dec 2011.

[2] S. A. Murray, K. H. Ha, C. Hartigan, and M. Goldfarb, "An assistive control approach for a lower-limb exoskeleton to facilitate recovery of walking following stroke," *IEEE Trans. Neural Syst. Rehabil. Eng.*, vol. 23, no. 3, pp. 441–449, 2015.

[3] "Mobility is Most Common Disability Among Older Americans, Census Bureau Reports," 2014. [Online]. Available: http://www.census.gov/newsroom/press-releases/2014/cb14-218.html.

[4] United States Bone and Joint Initiative, *The Burden of Musculoskeletal Diseases in the United States*, 3rd ed., 2014. [Online]. Available: http://www.boneandjointburden.org/

[5] S. Amin, K. Baker, J. Niu, M. Clancy, J. Goggins, A. Guermazi, M. Grigoryan, D. J. Hunter, and D. T. Felson, "Quadriceps strength and the risk of cartilage loss and symptom progression in knee osteoarthritis," *Arthritis and Rheumatism*, 2009.

[6] A. H. Alnahdi, J. A. Zeni, and L. Snyder-Mackler, "Muscle Impairments in Patients With Knee Osteoarthritis," *Sports Health*, 2012.

[7] S. M. Hsiang, G. E. Brogmus, and T. K. Courtney, "Low back pain (LBP) and lifting technique–A review," *International Journal of Industrial Ergonomics*, vol. 4, no. 19, pp. 59–74, 1997.

[8] H. Kaminaga, T. Amari, Y. Niwa, and Y. Nakamura, "Development of knee power assist using backdrivable electro-hydrostatic actuator," in *IEEE Int. Conf. Intelligent Robots & Systems*, 2010, pp. 5517–5524.

[9] K. Kong, J. Bae, and M. Tomizuka, "Control of rotary series elastic actuator for ideal force-mode actuation in human–robot interaction applications," *IEEE/ASME Trans. Mechatronics*, vol. 14, no. 1, pp. 105–118, 2009.

[10] ——, "A compact rotary series elastic actuator for human assistive systems," *IEEE/ASME Trans. Mechatronics*, vol. 17, no. 2, pp. 288–297, 2012.

[11] D. Accoto, G. Carpino, F. Sergi, N. L. Tagliamonte, L. Zollo, and E. Guglielmelli, "Design and characterization of a novel high-power series elastic actuator for a lower limb robotic orthosis," *International Journal of Advanced Robotic Systems*, vol. 10, 2013.

[12] M. K. Shepherd and E. J. Rouse, "Design and validation of a torque-controllable knee exoskeleton for sit-to-stand assistance," *IEEE/ASME Transactions on Mechatronics*, vol. 22, no. 4, pp. 1695–1704, 2017.

[13] H. Yu, M. Sta Cruz, G. Chen, S. Huang, C. Zhu, E. Chew, Y. S. Ng, and N. V. Thakor, "Mechanical design of a portable knee-ankle-foot robot," in *IEEE Int. Conf. Robot. Autom.*, 2013, pp. 2183–2188.

[14] B. Brackx, J. Geeroms, J. Vantilt, V. Grosu, K. Junius, H. Cuypers, B. Vanderborght, and D. Lefeber, "Design of a modular add-on compliant actuator to convert an orthosis into an assistive exoskeleton," in *IEEE Int. Conf. Biomed. Robot. Biomechatron.*, 2014, pp. 485–490.

[15] C. Lagoda, A. C. Schou, A. H. Stienen, E. E. Hekman, and H. van der Kooij, "Design of an electric series elastic actuated joint for robotic gait rehabilitation training," in *IEEE Int. Conf. Biomed. Robot. Biomechatron.*, 2010, pp. 21–26.

[16] D. W. Robinson, "Design and analysis of series elasticity in closed-loop actuator force control," Ph.D. dissertation, Massachusetts Institute of Technology, 2000.

[17] S. Seok, A. Wang, M. Y. M. Chuah, D. J. Hyun, J. Lee, D. M. Otten, J. H. Lang, and S. Kim, "Design principles for energy-efficient legged locomotion and implementation on the MIT Cheetah robot," *IEEE/ASME Trans. Mechatron.*, vol. 20, no. 3, pp. 1117–1129, 2015.

[18] G. Kenneally, A. De, and D. Koditschek, "Design principles for a family of direct-drive legged robots," *IEEE Robotics and Automation Letters*, vol. 1, no. 2, pp. 900–907, 2016.

[19] Y. Ding and H.-W. Park, "Design and experimental implementation of a quasi-direct-drive leg for optimized jumping," in *IEEE/RSJ Int. Conf. Intelligent Robots & Systems*, 2017.

[20] N. Paine and L. Sentis, "Design and comparative analysis of a retrofitted liquid cooling system for high-power actuators," *Actuators*, vol. 4, no. 3, pp. 182–202, 2015.

[21] H. Zhu, J. Doan, C. Stence, G. Lv, T. Elery, and R. Gregg, "Design and validation of a torque dense, highly backdrivable powered knee-ankle orthosis," in *IEEE International Conference on Robotics and Automation*, 2017, pp. 504–510.

[22] G. Lv, H. Zhu, and R. D. Gregg, "On the design and control of highly backdrivable lower-limb exoskeletons," *IEEE Control Systems Magazine*, vol. 38, no. 6, pp. 88–113, Dec 2018.

[23] J. Wang, X. Li, T. Huang, S. Yu, Y. Li, T. Chen, A. Carriero, M. Oh-Park, and H. Su, "Comfort-centered design of a lightweight and backdrivable knee exoskeleton," *IEEE Robotics and Automation Letters*, vol. 3, no. 4, pp. 4265–4272, Oct 2018.

[24] G. Lv, H. Zhu, T. Elery, L. Li, and R. D. Gregg, "Experimental implementation of underactuated potential energy shaping on a powered ankle-foot orthosis," in *IEEE Int. Conf. Robot. Autom.*, 2016, pp. 3493–3500.

[25] T. Elery, S. Rezazadeh, C. Nesler, J. Doan, H. Zhu, and R. D. Gregg, "Design and benchtop validation of a powered knee-ankle prosthesis with high-torque, low-impedance actuators," in *IEEE International Conference on Robotics and Automation*, 2018.

[26] J. Ramos, B. Katz, M. Y. M. Chuah, and S. Kim, "Facilitating model-based control through software-hardware co-design," in *IEEE Int. Conf. Robot. Autom.*, May 2018, pp. 566–572.

[27] H. Li, K. W. Klontz, V. E. Ferrell, and D. Barber, "Thermal models and electrical machine performance improvement using encapsulation material," *IEEE Transactions on Industry Applications*, vol. 53, no. 2, pp. 1063–1069, 2017.

[28] J. L. Astephen, K. J. Deluzio, G. E. Caldwell, and M. J. Dunbar, "Biomechanical changes at the hip, knee, and ankle joints during gait are associated with knee osteoarthritis severity," *Journal of Orthopaedic Research*, vol. 26, no. 3, pp. 332–341, 2008.

[29] M. Antwi-Afari, H. Li, D. Edwards, E. Prn, J. Seo, and A. Wong, "Biomechanical analysis of risk factors for work-related musculoskeletal disorders during repetitive lifting task in construction workers," *Automation in Construction*, vol. 83, pp. 41–47, 2017.

[30] J. A. Neder, L. E. Nery, G. T. Shinzato, M. S. Andrade, C. Peres, and A. C. Silva, "Reference values for concentric knee isokinetic strength and power in nonathletic men and women from 20 to 80 years old," *J. Orthop. Sport Phys.*, vol. 29, no. 2, pp. 116–126, 1999.

[31] J. W. Sensinger, S. D. Clark, and J. F. Schorsch, "Exterior vs. interior rotors in robotic brushless motors," in *IEEE International Conference on Robotics and Automation*, 2011, pp. 2764–2770.

[32] J. W. Sensinger and J. H. Lipsey, "Cycloid vs. harmonic drives for use in high ratio, single stage robotic transmissions," in *IEEE International Conference on Robotics and Automation*. IEEE, 2012, pp. 4130–4135.

[33] J. Yang, D. Liang, D. Yu, and T. Y. F. Lang, "System identification and sliding mode control design for electromechanical actuator with harmonic gear drive," in *Chinese Control and Decision Conference*. IEEE, 2016, pp. 5641–5645.

[34] S. Molian, *Mechanism design: an introductory text*. Cambridge University Press, 1982.

[35] C. R. Sullivan and S. R. Sanders, "Models for induction machines with magnetic saturation of the main flux path," in *IEEE Industry Applications Society Annual Meeting*. IEEE, 1992, pp. 123–131.

[36] W. Qiao, R. G. Harley *et al.*, "Control of ipm synchronous generator for maximum wind power generation considering magnetic saturation," *IEEE Trans. Industry Applications*, vol. 45, no. 3, pp. 1095–1105, 2009.

[37] W. P. Kelleher and A. S. Kondoleon, "A magnetic bearing suspension system for high temperature gas turbine applications: Part iii–magnetic actuator development," in *ASME Int. Gas Turbine and Aeroengine Congress and Exhibition*, 1997, p. V004T14A030.

[38] A. M. El-Refaie, "Fractional-slot concentrated-windings synchronous permanent magnet machines: Opportunities and challenges," *IEEE Trans. Industrial Electronics*, vol. 57, no. 1, pp. 107–121, 2010.

[39] G. Lv and R. D. Gregg, "Underactuated potential energy shaping with contact constraints: Application to a powered knee-ankle orthosis," *IEEE Trans. Control Syst. Technol.*, vol. 26, no. 1, pp. 181–193, 2018.

[40] E. J. Rouse, R. D. Gregg, L. J. Hargrove, and J. W. Sensinger, "The difference between stiffness and quasi-stiffness in the context of biomechanical modeling," *IEEE Transactions on Biomedical Engineering*, vol. 60, no. 2, pp. 562–568, 2013.

[41] K. Shamaei, P. C. Napolitano, and A. M. Dollar, "Design and functional evaluation of a quasi-passive compliant stance control knee–ankle–foot orthosis," *IEEE Trans. Neural Systems and Rehabilitation Engineering*, vol. 22, no. 2, pp. 258–268, 2014.

[42] G. F. Franklin, J. D. Powell, and A. Emami-Naeini, *Feedback Control of Dynamic Systems*, 7th ed. New York, NY: Pearson, 2014.